communications physics

ARTICLE

https://doi.org/10.1038/s42005-022-00921-3 OPEN

Layer-dependent magnetic phase diagram in Fe_nGeTe_2 ($3 \leq n \leq 7$) ultrathin films

Qinxi Liu[1], Jianpei Xing[1], Zhou Jiang[1], Yu Guo[1], Xue Jiang[1✉], Yan Qi[1,2✉] & Jijun Zhao[1]

Two-dimensional (2D) ferromagnets with high Curie temperature T_C are desirable for spintronics applications. However, they are rarely obtained in experiments mainly due to the challenge of synthesizing high-quality 2D crystals, and their T_C values are below room temperature. Using first-principles calculations, we design a family of stable 2D Fe_nGeTe_2 ($4 \leq n \leq 7$) ultrathin films with coexisting itinerant and localized magnetism. Among them, 2D Fe_3GeTe_2 and Fe_4GeTe_2 are ferromagnetic metals with $T_C = 138$ and 68 K; 2D Fe_5GeTe_2, Fe_6GeTe_2, and Fe_7GeTe_2 are Néel's P-, R-, and R-type ferrimagnetic metals with $T_C = 320$, 450, and 570 K. A thickness-induced magnetic phase transition originates from competition between itinerant and localized states, and also correlates with Fe^{3+} and Fe^{2+} content. A valence/orbital-dependent magnetic exchange model is proposed for these effects. Our results reveal a universal mechanism for magnetic coupling in complex magnetic systems.

[1] Key Laboratory of Material Modification by Laser, Ion and Electron Beams (Dalian University of Technology), Ministry of Education, Dalian 116024, China. [2] School of Physics and Materials Engineering, Dalian Minzu University, Dalian 116600, China. ✉email: jiangx@dlut.edu.cn; qiyan@dlnu.edu.cn

Since the first successful exfoliation of monolayer CrI_3 and bilayer $CrGeTe_3$ sheets, the family of 2D magnetic materials has undergone tremendous growth during the past few years. At present, the range of 2D magnets covers insulators, semiconductors, half-metals, and metals. Among these, those of most interest are ferromagnetic (FM) semiconductors, such as CrX_3, NiX_3, $CrGeTe_3$, and RuX_3 (X = Cl, Br and I)[1–6]. Magnetism in these compounds originates from localized *d* electrons, and the magnetic ordering is usually mediated by superexchange interaction between the magnetic ions through the nonmetal atoms. The semi-empirical Goodenough–Kanamori–Anderson (GKA) rules provide a valuable picture to describe the magnetic interactions in these 2D compounds[7–9]. According to the GKA rules, the ferromagnetism in 2D semiconductors is mainly derived from 90° *d*–*p*–*d* superexchange. In this situation, the occupied orbitals overlap with different orthogonal *p* orbitals of a ligand. It is thus not surprising that weak ferromagnetism is usually found in these systems. As representatives, the observed Curie temperatures T_C of the 2D compounds CrI_3 and $CrGeTe_3$ are 45 K and 30 K, respectively, which are far below room temperature[1,4].

As well as these FM semiconductors, metallic ferromagnets are another important class of 2D ferromagnets. A significant advantage of metallic ferromagnets is that their metallic nature enables an interplay between spin and charge degrees of freedom, which are the main concern in spintronics[10]. The reported metallic ferromagnets, such as $CrTe_x$, Cr_2BC, $FeSe_2$, FeTe, MnSe, and Fe_nGeTe_2, exhibit robust ferromagnetism with high T_C (130–846 K)[11–21]. In particular, 2D metallic Fe–Ge–Te ternary (FGT) compounds with high T_C and huge magnetic anisotropy energy (MAE) along the *c* axis have attracted attention. Among FGT thin films, 2D Fe_3GeTe_2 was first obtained by cleaving Fe_3GeTe_2 bulk crystal onto a gold film evaporated on top of an SiO_2/Si substrate. The polar reflective magnetic circular dichroism measurement confirmed that the T_C was preserved at 68–130 K, with an MAE value of ~2.0 meV at the monolayer limit[13,14]. Subsequently, Kim et al.[15] successfully synthesized and exfoliated seven-layer Fe_4GeTe_2 flakes with 7 nm thickness and determined that the T_C was about 270 K. However, the observed MAE was reduced from 1.03 to 0.23 $J\ cm^{-3}$ when the composition changed from Fe_3GeTe_2 to Fe_4GeTe_2[15]. Another important member of the FGT family is Fe_5GeTe_2, and mechanically exfoliated $Fe_{5-x}GeTe_2$ nanoflakes have been found to be metallic ferromagnets with a high T_C of 270–332 K[16,22].

Spontaneous magnetization in most 2D metallic ferromagnets is generally accepted to be due to itinerant electrons, which can be understood in terms of the well-known Stoner model[23]. The electrons behave ferromagnetic just because of their repulsive Coulomb interaction, while the contributions from lattice and band structure are totally ignored. Beneficial from the delocalized electrons, most of the reported metallic ferromagnets have higher T_C than FM semiconductors. However, there is a considerable amount of evidence suggesting that metallic FGT systems are not conventional Stoner ferromagnets[14,24,25]. Itinerant magnetism cannot fully explain the variation of T_C in FGT systems. For example, Dai et al.[24] found that increased hydrostatic pressure led to enhanced electron itinerancy but decreased T_C in thin Fe_3GeTe_2 flakes. Yang et al.[25] noted that the band dispersions of Fe_3GeTe_2 barely changed upon heating towards the ferromagnetic transition near 225 K, which also represents a strong deviation from the itinerant Stoner model. Deng et al.[14] used the localized Heisenberg model to estimate the magnetic properties of 2D Fe_3GeTe_2, which were consistent with experimental results. All these results suggest that local magnetic moments may play a crucial role in the FM ordering of Fe–Ge–Te systems. From the above experimental reports, we can conclude that 2D metallic FGT compounds are prospective candidates for room-temperature ferromagnets. However, there remain several unresolved issues, such as the physical origin of the localized magnetism in these metallic systems, the validity of the Stoner model and the Heisenberg model, the effects of composition and thickness, and the influence of magnetic anisotropy.

To resolve these issues, the electronic and magnetic properties of 2D Fe_3GeTe_2 are systemically investigated in this work. We find that the five 3*d* orbitals of 2D Fe_3GeTe_2 can be divided into two parts: there are a_1 (d_{z^2}) states that are mostly localized on the Fe sites and give rise to local spin moments, whereas the other e_1 ($d_{xy}/d_{x^2-y^2}$) and e_2 (d_{xz}/d_{yz}) states are itinerant. According to the orbital occupation behavior of the localized a_1 (d_{z^2}) states and the different coordination environments, we infer the valence states of Fe atoms in Fe_3GeTe_2 are +2 and +3, respectively. For localized spins on Fe atoms, we propose a valence-dependent multipath magnetic coupling mechanism to describe the competition between the interlayer ferromagnetism and antiferromagnetism, while the itinerant e_1 and e_2 states always favor intra- and interlayer ferromagnetism in 2D Fe_3GeTe_2. Furthermore, the MAE also depends on the valence state of the Fe ions and originates from the coupling between a_1 and e_2 states. Based on these findings, we construct a series of 2D Fe_nGeTe_2 ultrathin films ($4 \leq n \leq 7$) with different Fe contents and thicknesses. The combined effects of these differences on magnetic moment, magnetic exchange parameters, and MAE are discussed. We find that the T_C value of Fe_nGeTe_2 ultrathin films does indeed depend on the competition between localization and itinerant magnetism. Interesting thickness-induced magnetic phase transformations from ferromagnetism to Néel's P-type ferrimagnetism and then to R-type ferrimagnetism are observed in 2D Fe_nGeTe_2 films, whose T_C are in the range of 68–570 K. Our results not only reveal a route for the design of 2D intrinsic magnets with high Curie temperature, but also provide a universal theoretical model for analyzing the itinerant and localized magnetism in complex materials.

Results

Coexistence of localized and itinerant magnetism in 2D Fe_3GeTe_2. The atomic configuration of 2D Fe_3GeTe_2 is shown in Fig. 1. Each Fe_3GeTe_2 unit has a thickness of five atomic layers. Clearly, there are two types of Fe atoms with different coordination environments, namely, trivalent iron (Fe^{3+}) and divalent iron (Fe^{2+}). The middle of the 2D Fe_3GeTe_2 is a Fe^{2+}Ge layer, sandwiched by bottom and top Fe^{3+} layers. The entire surface of each Fe^{3+} layer is then covered by an atomic layer of Te. The corresponding ratio of number of Fe^{3+} and Fe^{2+} is 2:1. The 2D Fe_3GeTe_2 is metallic[13], as can be seen from both the electronic band structure and the total density of states (TDOS) in Supplementary Note 1. Nonmagnetic (NM), FM, and antiferromagnetic (AFM) states are all considered, to determine their ground spin configurations. The corresponding FM and various AFM configurations are shown in Supplementary Note 2. Our results indicate that 2D Fe_3GeTe_2 has an FM ground state.

In addition to their coordination environment, the Fe^{3+} and Fe^{2+} ions are more accurately distinguished in 2D Fe_3GeTe_2 by their different electronic behaviors, which is confirmed by the charge density distributions and the Bader charge on Fe atoms[26] (see Supplementary Notes 1 and 4) Electrons are more strongly localized around the Fe^{2+} ions than around the Fe^{3+} sites. The electrons are localized between Fe^{2+} and Ge/Te ions, indicating covalent bonding characteristics. By comparison, more delocalized ionic bonding takes place between Fe^{3+} and Ge/Te ions. This difference between localized and delocalized electron

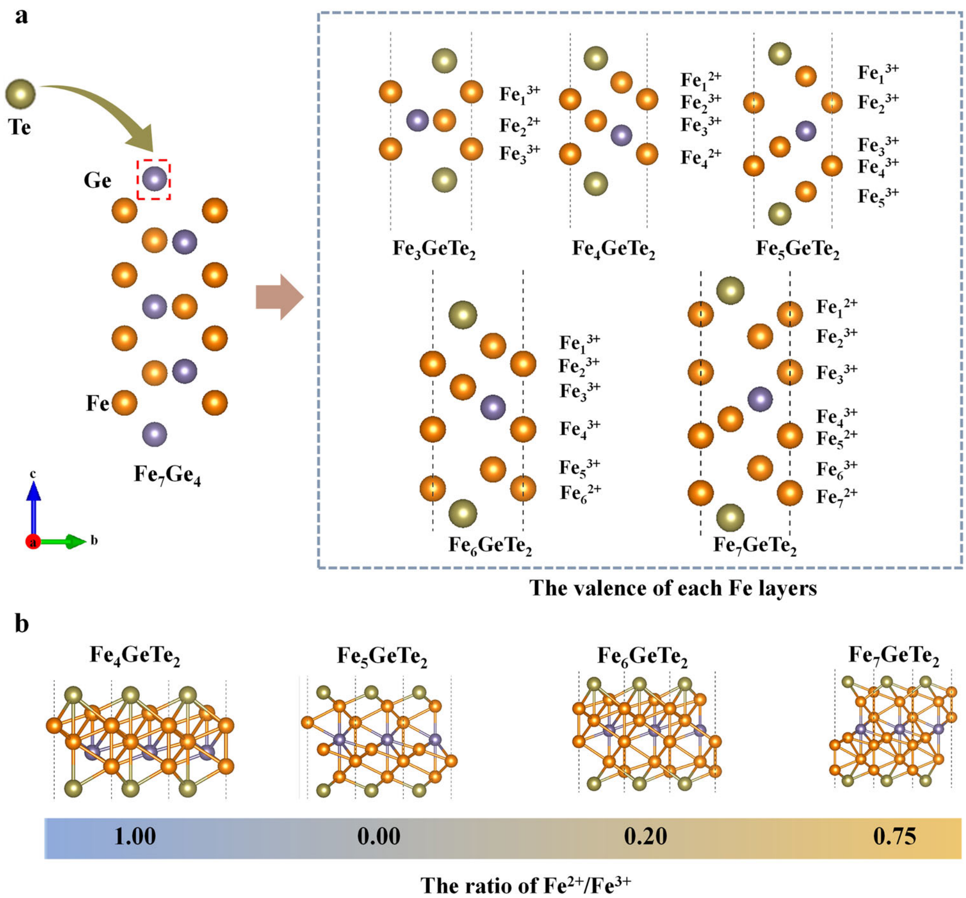

Fig. 1 Crystal structure of Fe_nGeTe_2 ($4 \leq n \leq 7$). **a** Schematic illustration of Te-substituted Fe_7Ge_4 crystal and of five structures in the series Fe_nGeTe_2. The green, purple and gold spheres correspond to Te, Ge, and Fe atoms, respectively. **b** Stacked plane views along the [001] direction of Fe_nGeTe_2 multilayer films with different Fe^{2+}/Fe^{3+} ratios.

distributions around the Fe^{3+} and Fe^{2+} ions is also supported by deformation charge density analysis and Bader charge (see Supplementary Fig. 2 and Note 4). There is a net charge transfer of about 0.4 electron from each Fe^{3+} ion to its surrounding Ge/Te ions. However, there is no evident charge transfer in the case of Fe^{2+} ions. Following this picture, we find that the Fe^{2+} ions are localized relative to the Fe^{3+} ions in 2D Fe_3GeTe_2, which is consistent with a previous report by ref. [27]. The coexistence of localized and itinerant magnetism has also been found in iron-based superconductors and double perovskite materials, such as LaOFeAs, Sr_2FeMoO_6, and $La_{1-x}Sr_xMO_3$ (M = Mn and Co)[28–31], all of which are polyvalent materials.

The partial density of states (PDOS) can provide further clarification of the origin of different electronic and magnetic features in Fe^{3+} and Fe^{2+} ions of 2D Fe_3GeTe_2, which are shown in Supplementary Note 1. Under a hexagonal crystal field, the five 3*d* orbitals of the Fe atom split into a single state a_1 (d_{z^2}), two twofold-degenerate states e_1 ($d_{x^2-y^2}/d_{xy}$) and e_2 (d_{xz}/d_{yz}). From the PDOS of Fe atoms, one can see that the d_{z^2} orbital is clearly narrower and sharper than the other 3*d* orbitals, suggesting a localized feature. However, it is also obvious that the $d_{x^2-y^2}$, d_{xy}, d_{xz}, and d_{yz} orbitals in the minority-spin channels are obviously wide and are hybridized with Ge/Te-*p* states, indicating a delocalized feature. Similar to LaOFeAs, the localized *d* electrons differ from the itinerant electrons in coming from more isolated d_{z^2} orbitals[28]. Moreover, the 3*d* bands of the majority spin for both Fe^{3+} and Fe^{2+} ions are fully occupied, while those of the minority spin are partially occupied.

Based on the occupation matrix, the electron occupation numbers of the d_{z^2}, $d_{x^2-y^2}$, d_{xy}, d_{xz}, and d_{yz} orbitals of Fe_nGeTe ultrathin films are listed in Supplementary Note 4, which further confirms the valance states of Fe ions. The main difference between Fe^{3+} and Fe^{2+} ions in terms of the PDOS is due to the d_{z^2} and d_{xz}/d_{yz} states in the minority-spin channels. Specifically, the electron occupation numbers in the minority d_{z^2} orbitals are 0.04 and 0.30 for Fe^{3+} and Fe^{2+} ions, respectively. That is to say, the Fe^{2+} ion has ~0.3 more electrons than Fe^{3+} ion to occupy the minority d_{z^2} orbital. The occupied minority d_{z^2} orbital results in the Fe^{2+} ion being more localized than the Fe^{3+} ion. In addition, compared with the Fe^{2+} ion, the energy level of the minority d_{xz}/d_{yz} state of the Fe^{3+} ion will shift to lower energy. The corresponding number of occupied minority d_{xz}/d_{yz} states increases from 0.35 to 0.54. Therefore, the resulting calculated net magnetic moments are 3.0 μ_B and 2.6 μ_B for Fe^{3+} and Fe^{2+} ions, respectively. Similar to Fe ion in Li_3FeN_3, $(PMe_3)_2FeCl_3$ and $FePc/Ti_3C_2T_x$ compounds[32–34], the magnetic moments values may suggest that both Fe^{3+} and Fe^{2+} ions are probably in their intermediate spin states. The intermediate-spin state can become the ground states of the system due to the relative stability of the ligand hole states that it hybridizes with ref. [35] A density functional theory (DFT) calculation by Zhu et al.[36] gave similar values of 2.5 μ_B and 1.6 μ_B for the magnetic moments of Fe^{3+} and Fe^{2+} ions, respectively, in bulk Fe_3GeTe_2. The localized a_1 and delocalized e_1/e_2 states result in the unique magnetic properties of 2D Fe_3GeTe_2, with coexistence of local and itinerant magnetism, consistent with a previous report by ref. [25]

Magnetic coupling mechanism of 2D Fe_3GeTe_2. Because of the coexistence of localized and itinerant magnetism, the magnetic behavior of metallic ferromagnetic Fe_3GeTe_2 will deviate from the itinerant Stoner model. The recent experiment by Yang et al.[25] indeed confirmed that metallic Fe_3GeTe_2 exhibits non-Stoner ferromagnetism. Yang et al. did not observe any considerable change in electronic structure with temperature, which is not consistent with expectations. According to the itinerant Stoner model, a ferromagnetic metal will exhibit a temperature-dependent exchange splitting that disappears above T_C[25]. Moreover, Tovar et al.[29] used a corrected Stoner parameter to describe the magnetic behaver in polyvalent Sr_2FeMoO_6 and found evidence for the coexistence of localized and itinerant magnetism in this material too. The corrections for Landau diamagnetism to the Stoner parameter need to derived from experimental measurements[29]. Therefore, we need a new model to describe the complicated ferromagnetism in Fe_3GeTe_2 systems.

In this paper, two main magnetic exchange mechanisms have been introduced in 2D Fe_3GeTe_2, namely, the itinerant magnetism between e_1 and e_2 electrons and the localized magnetism in a_1 spins. Therefore, we propose a multipath magnetic interaction mechanism to understand the localized magnetic exchange in 2D Fe_3GeTe_2. According to the splitting of Fe^{2+} and Fe^{3+} orbitals in the crystal field and the multilayer structure of 2D Fe_3GeTe_2, three possible exchange paths are considered. Figure 2 shows the exchange paths between unoccupied d_{z^2} orbitals (Fe^{3+}–Fe^{3+}), between occupied d_{z^2} orbitals (Fe^{2+}–Fe^{2+}), and from an unoccupied to an occupied d_{z^2} orbital (Fe^{2+}–Fe^{3+}), respectively. The hopping from an occupied Fe-d_{z^2} orbital to an unoccupied Fe-d_{z^2} orbitals induces extremely strong FM coupling (path $\boldsymbol{P_1}$), which occurs between magnetic ions in different oxidation states, i.e., double exchange[37]. Double exchange plays an essential role in polyvalent ferromagnetic materials such as $La_{1-x}Sr_xMnO_3$ that also exhibit both localized and itinerant magnetism[38]. However, spin crossover between both unpaired Fe-d_{z^2} orbitals (path $\boldsymbol{P_2}$) and paired Fe-d_{z^2} orbitals (path $\boldsymbol{P_3}$) gives rise to an AFM interaction according to the Pauli exclusion principle. On the other hand, the non-spin-polarized PDOS (see Supplementary Note 1) shows that d_{xz}/d_{yz} and $d_{x^2-y^2}/d_{xy}$ are mainly contributed at the Fermi level, and their lower kinetic energy makes them contribute to the itinerant ferromagnetism in 2D Fe_3GeTe_2. Therefore, the interaction between itinerant electrons in e_1 states favors intralayer FM ($\boldsymbol{I_1}$), while the coupling between electrons in e_2 states favors interlayer FM ($\boldsymbol{I_2}$). Of these, the intralayer FM is contributed only by itinerant electrons ($\boldsymbol{I_1}$), but there is competition between interlayer FM ($\boldsymbol{P_1}$ and $\boldsymbol{I_2}$) and AFM ($\boldsymbol{P_2}$ and $\boldsymbol{P_3}$) coupling. This explains why there is some debate regarding Fe atoms behaving ferromagnetically or antiferromagnetically in Fe_3GeTe_2[39]. Moreover, Fu et al.[40] have also found that the coexistence of localized and itinerant 3*d* electrons in $BiFeO_3$/$SrTiO_3$ superlattices and itinerant Fe-3*d* electrons tends to cause ferromagnetism.

A local Heisenberg model can provide a good description of the FM ordering in the Fe_3GeTe_2 system[14]. In 2D Fe_3GeTe_2, there are three types of exchange interaction between Fe ions, corresponding to the first, second, and third nearest neighbor magnetic exchange constants J_1, J_2, and J_3, as shown in Fig. 2. The values of J_1, J_2, and J_3 for 2D Fe_3GeTe_2 can be extracted from the total energy difference between different spin orderings. As summarized in Table 1, the derived exchange interaction parameters are $J_1 = -0.44$ meV, $J_2 = 3.27$ meV, and $J_3 = 0.47$ meV. It is known that a positive *J* value favors FM ordering, while a negative *J* value favors AFM coupling. Therefore, the calculated J_1 of -0.44 meV yields weak AFM coupling, which occurs mainly through the path $\boldsymbol{P_2}$. The path $\boldsymbol{P_1}$ corresponds to strong FM coupling, with J_2 having a value of 3.27 meV. Moreover, itinerant magnetism ($\boldsymbol{I_1}$ and $\boldsymbol{I_2}$) gives a value of 0.47 meV for J_3, corresponding to long-range intralayer FM coupling. The coincidence between the magnetic interaction parameters and the effect of coexisting localized and itinerant magnetism suggests that our proposed magnetic interaction mechanism is valid for understanding the magnetic ground state of 2D Fe_3GeTe_2. Its validity is also verified by other theoretical results. For example, first-principles calculations by Hu et al.[41] have shown that the stability of ferromagnetism can be greatly enhanced by tensile strain in Fe_3GeTe_2 monolayer. According to our picture, tensile strain will shorten the Fe^{3+}–Fe^{2+} distance ($\boldsymbol{P_1}$ path) but lengthen the other interatomic distances, which in turn will enhance FM double exchange between Fe^{3+} and Fe^{2+} ions.

MAE as an important parameter of ferromagnets counteracts thermal fluctuations and preserves long-range FM ordering[42]. From noncollinear calculations with inclusion of the spin–orbit coupling (SOC) effect, the MAE of 2D Fe_3GeTe_2 has been determined as 0.94 meV/Fe, favoring perpendicular anisotropy, whereas the previously reported value was 0.67 meV/Fe[14]. For comparison, the MAE of 2.5 meV/Fe in bulk Fe_3GeTe_2 is slightly higher. The physical origin of a positive MAE can be ascribed to the matrix element differences between the occupied and unoccupied spin-down *d* orbitals of the Fe atom[43]. For the contributions from *d* electrons, all nonvanishing matrix elements will make nonnegligible contributions to the MAE. In a simple analysis, the matrix elements that are near the Fermi level in spin-down states are most important to the MAE. According to Eq. (4) in the Methods section, the contribution to MAE is dominated by the coupling of $\langle xz, |, L_z, |, yz\rangle$ and $\langle xz, yz, |, L_x, |, z^2\rangle$. Owing to the degeneracy of the d_{xz} and d_{yz} orbitals, we consider mainly the coupling between d_{z^2} and d_{xz}/d_{yz} orbitals. Roughly speaking, the positive contributions to the total MAE originate mainly from unoccupied d_{z^2} orbitals and half-occupied d_{xz}/d_{yz} orbitals of Fe^{3+} ions, while the coupling of occupied d_{z^2} and unoccupied d_{xz}/d_{yz} orbitals of Fe^{2+} ions make a negative contribution to the MAE. Such a mechanism also accounts for the variation in MAE for Fe_3GeTe_2 monolayer when the Fe^{3+} content is decreased by hole doping, as observed by Park et al.[44].

An experimental study by Hwang et al.[45] found AFM coupling between pristine Fe_3GeTe_2 layer and oxidized Fe_3GeTe_2 layers. Their DFT calculations further revealed that such AFM coupling mainly originates from the oxygen atoms located at the bilayer interface, while bilayer Fe_3GeTe_2 with oxygen atoms adsorbed on the top or bottom sites still preferentially exhibit an FM state. According to our localized Fe–Fe exchange model, the intermediate oxygen atoms could provide an oxygen-mediated $\boldsymbol{P_2}$ path between two Fe_3GeTe_2 layers, thereby inducing AFM coupling. Dai et al.[24] reported a pressure-dependent phase diagram of Fe_3GeTe_2 thin flakes, with a magnetic transformation temperature from ferromagnetic to paramagnetic states of 203 K at 3.7 GPa and 163 K at 7.3 GPa. Moreover, the T_C showed a clear decreasing trend from 4.0 GPa to 7.3 GPa because of the reduced local magnetic moment and increased electronic itinerancy. On the one hand, the increased electronic itinerancy could weaken the localized double exchange ($\boldsymbol{P_1}$ path). On the other hand, by analyzing structural characteristics, we found that the Fe^{3+}–Te distance clearly decreases at pressures below 7 GPa. The corresponding Fe^{3+}–Fe^{3+} exchange though the Te-mediated $\boldsymbol{P_2}$ path is stronger. As a consequence of the weakened FM coupling and enhanced AFM coupling, T_C is drastically reduced. In particular, the gate-tunable electrons sequentially fill the subband origin from the Fe-d_{z^2}, d_{xz}, and d_{yz} orbitals, inducing room-temperature ferromagnetism in Fe_3GeTe_2[14]. The value of T_C depends mainly on the interaction between d_{z^2}, d_{xz}, and d_{yz}

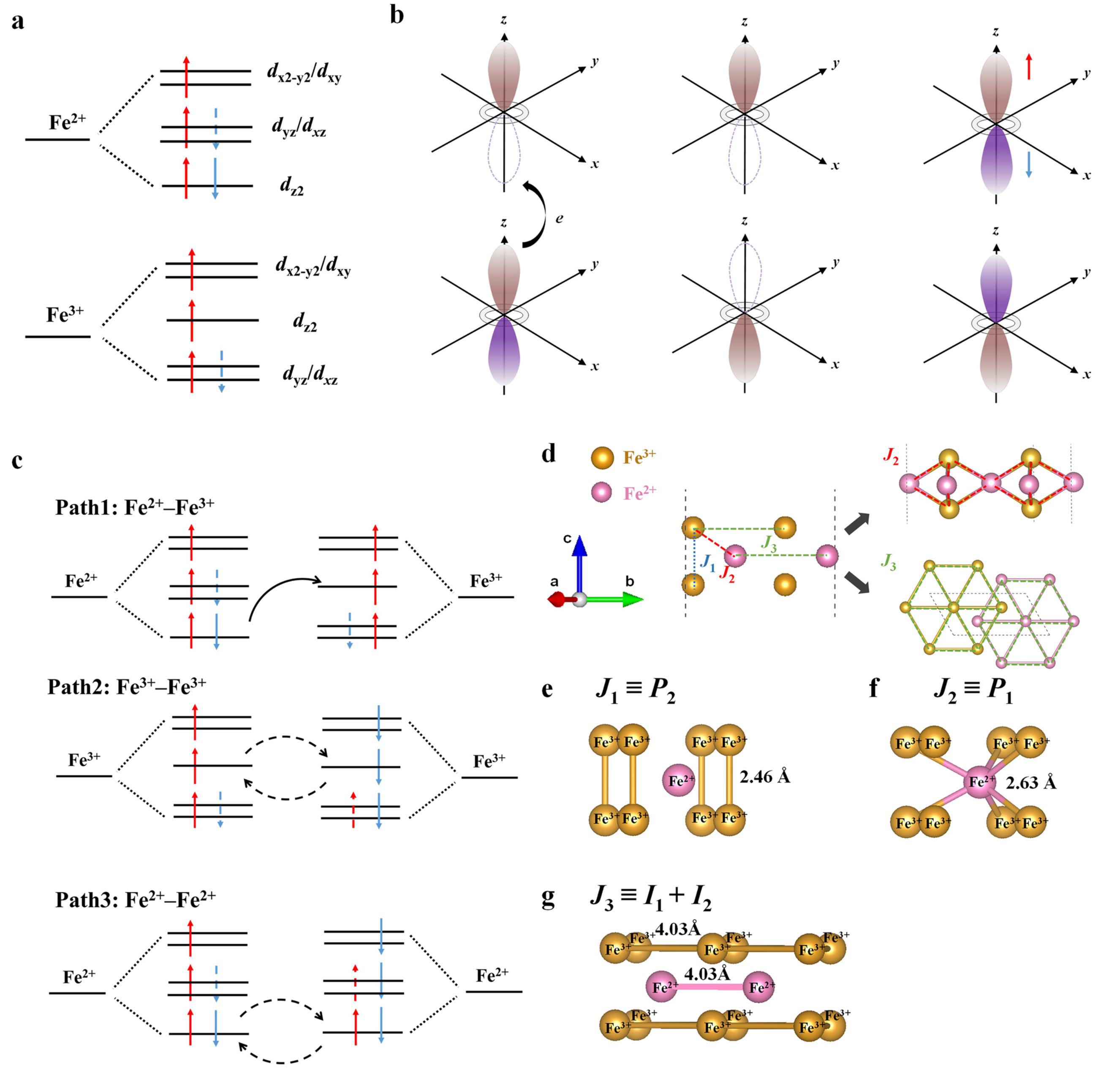

Fig. 2 Magnetic exchange interaction in 2D Fe_3GeTe_2. **a** Schematic representation of the splitting of *d* orbitals in Fe^{2+} and Fe^{3+} ions, respectively. **b** Three possible processes for the exchange between localized d_{z^2} orbitals. **c** The corresponding three possible localized Fe–Fe exchange paths in the Fe_3GeTe_2 crystal. **d** Side view showing the magnetic exchange parameters J_1, J_2, and J_3 for the Fe–Fe coupling in Fe_3GeTe_2 crystal, together with the Fe–Fe exchange interaction paths for these parameters in monolayer Fe_3GeTe_2. **e–g** Schematic representations of the exchange parameters J_1, J_2, and J_3, respectively.

Table 1 Structure and magnetic parameters in 2D Fe_nGeTe_2 ($4 \leq n \leq 7$).

	x	Thickness (Å)	E_{form} (eV/atom)	M (μ_B)	MAE (meV)	T_C (K)	Exchange parameter (meV) J_1	J_2	J_3
Fe_3GeTe_2	0.5	8.61	−0.08	2.87	2.83	138	−0.44	3.27	0.47
Fe_4GeTe_2	1.0	9.10	−0.03	2.73	−5.01	68	7.40	10.50	0.10
Fe_5GeTe_2	0	10.95	−0.11	3.18	4.53	320	−0.20	4.70	−2.60
Fe_6GeTe_2	0.2	11.03	−0.05	2.94	6.31	450	6.60	−8.60	21.20
Fe_7GeTe_2	0.75	12.21	−0.01	2.91	3.91	570	−29.40	23.00	27.50

Fe^{2+}/Fe^{3+} ratio x, effective thickness, formation energy E_{form}, magnetic moment M per Fe atom, magnetic anisotropy energy (MAE) per unit cell, Curie temperature T_C, and exchange parameters J_1, J_2, and J_3 of Fe_nGeTe_2 multilayer films.

orbitals, consistent with our previous discussion. Moreover, the transition from itinerant to localized magnetism increases T_C, indicating that the FM coupling in Fe_3GeTe_2 comes mainly from localized double exchange ($\boldsymbol{P_1}$ path).

Structure and magnetic behavior of Fe_nGeTe_2 ultrathin films. The above discussions on the one hand again demonstrate the coexistence of itinerant and localized magnetism in the Fe_3GeTe_2 system. On the other hand, the interlayer competition between localized exchange coupling (paths $\boldsymbol{P_1}$, $\boldsymbol{P_2}$, and $\boldsymbol{P_3}$) and itinerant electrons ($\boldsymbol{I_1}$ and $\boldsymbol{I_2}$) is also crucial in determining the nature of the magnetic ground states and the values of the Curie temperature and MAE of 2D Fe_3GeTe_2. Moreover, T_C has been found to increase from 143 K to 226 K when the Fe content is increased from 2.75 to 3.10 in bulk $Fe_{3-x}GeTe_2$[46], indicating that T_C is very sensitive to Fe content. These findings motivate us to explore new high-temperature Fe–Ge–Te systems with optimal Fe^{2+}/Fe^{3+} ratio and thickness, in which the valences of Fe ions are related to the direction of MAE and the competition between localized and itinerant magnetism in the Fe_nGeTe_2 system. To satisfy these requirements, we have designed a series of Fe-rich Fe_nGeTe_2 ($4 \le n \le 7$) ultrathin films with various thicknesses (Fig. 1), which could exhibit abundant magnetism through more complicated competition between itinerant and localized magnetism in a multilayer structure. Similar to 2D Fe_3GeTe_2, these Fe_nGeTe_2 ultrathin films also belong to the *P*-3*m*1 space group. The effective thicknesses (Table 1) of Fe_4GeTe_2, Fe_5GeTe_2, Fe_6GeTe_2, and Fe_7GeTe_2 ultrathin films are 5.63 Å, 6.79 Å, 7.56 Å, and 8.73 Å, respectively, which are moderately larger than that of Fe_3GeTe_2 (5.14 Å). The atomic arrangements of Fe_nGeTe_2 ultrathin films can be regarded as six, seven, eight, and nine atomic layered thickness (001) surfaces of a Te-substituted Fe_7Ge_4 crystal[47]. Fortunately, the atomic arrangement of a five atomic layered thickness Te-substituted Fe_7Ge_4 crystal is the same as that of the experimentally reported Fe_3GeTe_2 phase.

To further check the experimentally feasibility of Fe_nGeTe_2, we have calculated their formation energies, defined as

$$E_f = [E(Fe_nGeTe_2) - E(Fe_2Ge) - E(Te_2) - (n-2)E(Fe)]/n, \quad (1)$$

where $E(Fe_nGeTe_2)$ is the total energy of the 2D Fe_nGeTe_2 compound, and $E(Fe_2Ge)$, $E(Te_2)$, and $E(Fe)$ are the total energies of Fe_2Ge, Te, and Fe in their most stable bulk phases[48]. The formation energies of four Fe_nGeTe_2 ultrathin films from our theoretical design are −0.03 eV/atom ($n = 4$), −0.11 eV/atom ($n = 5$), −0.05 eV/atom ($n = 6$), and −0.01 eV/atom ($n = 7$), which are comparable to the formation energy of −0.08 eV/atom for Fe_3GeTe_2. All these negative values indicate that the formation processes are exothermic. More importantly, we find that the total energy of our proposed Fe_5GeTe_2 ultrathin film is 0.24 eV per atom lower than that of the experimentally reported layered phase with the same stoichiometry[16]. It should be noted, however, that our DFT simulation results only mean that our proposed Fe_5GeTe_2 ultrathin film is energetically favorable than the experimentally reported one at 0 K. Anyway, the satisfactory stability of these Fe_nGeTe_2 ultrathin film implies that they are feasible from a theoretical point of view.

It is noteworthy that ultrathin films of Cr_2S_3, CrSe, and FeTe in a FM state have been synthesized by chemical vapor deposition and molecular beam epitaxy methods in previous experiments[11,12,49]. Therefore, we have proposed that our predicted Fe_nGeTe_2 films could be grown on the surface of hexagonal Si phase. The calculated lattice mismatches between Si(001) and (5×5) Fe_nGeTe_2 superlattices are 0.5%, 3.7%, 0.7%, and 1.1% for Fe_4GeTe_2, Fe_5GeTe_2, Fe_6GeTe_2, and Fe_7GeTe_2, respectively. The optimized structures of Fe_nGeTe_2/Si (001) heterostructures are shown in Supplementary Note 3. Evidently, the lattice misfit due to the Si substrate does not cause noticeable structural distortion in 2D Fe_nGeTe_2 superlattices.

We further discuss the electronic and magnetic properties of the proposed Fe_nGeTe_2 ultrathin films. Similar to 2D Fe_3GeTe_2, all the Fe_nGeTe_2 systems are metallic, as can be seen from the electronic band structures in Supplementary Fig. 6. The orbital projected densities of states in Supplementary Fig. 7 demonstrate that the metallicity still originates from *d* orbitals of Fe atoms. The coexistence of itinerant and localized *d* electrons in Fe_nGeTe_2 ($3 \le n \le 7$) can be revealed by the Bader charge (see Supplementary Note 4) and the PDOS. The distributions of Fe^{2+} and Fe^{3+} ions vary with the thickness and composition of the 2D Fe_nGeTe_2 ultrathin films. With increasing Fe content, the Fe^{2+}/Fe^{3+} (x) ratio is 0.5, 1.0, 0, 0.2, and 0.75 for $n = 3$, 4, 5, 6, and 7, respectively, which correspond to a progressive change in magnetic behavior from itinerant to localized. To investigate the ground states of Fe_nGeTe_2 ultrathin films, we consider FM and various AFM configurations (see Supplementary Fig. 8). Owing to the multilayer structure, the considered AFM configurations increase with increasing Fe content. From our DFT calculations, FM ordering in all Fe_nGeTe_2 systems is more favored than its AFM or NM counterparts. The magnetic moment as a function of x is plotted in Fig. 3a. With increasing Fe^{2+}/Fe^{3+} ratio, the average magnetic moment per Fe atom decreases slightly from 3.18 μ_B for $x = 0$ to 2.73 μ_B for $x = 1$. This observation can be easily understood on the basis that Fe^{3+} ions contribute a larger magnetic moment than Fe^{2+} ions.

Because the T_C in Fe_nGeTe_2 systems is determined mainly by localized double exchange, we consider the exchange parameters J of Fe_nGeTe_2 ultrathin films that are presented in Table 1 and Supplementary Note 5. Meanwhile, the long-range magnetic coupling with exchange parameter $J = 5$ instead of $J = 3$ is considered for Fe_nGeTe_2 ($n = 5$–7) with increasing Fe content

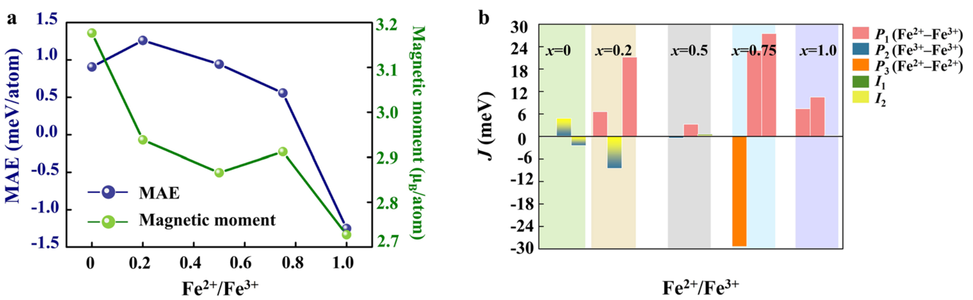

Fig. 3 Magnetic properties of multilayer Fe_nGeTe_2. a Calculated magnetic anisotropy energy (MAE) and magnetic moment per atom for various Fe^{2+}/Fe^{3+} ratios (x). The detailed data are listed in Table 1. **b** Exchange parameters for first, second, and third nearest neighbors (see Supplementary Fig. 9). The green, gold, gray, blue, and purple regions correspond to x = 0, 0.2, 0.5, 0.75, and 1.0, respectively.

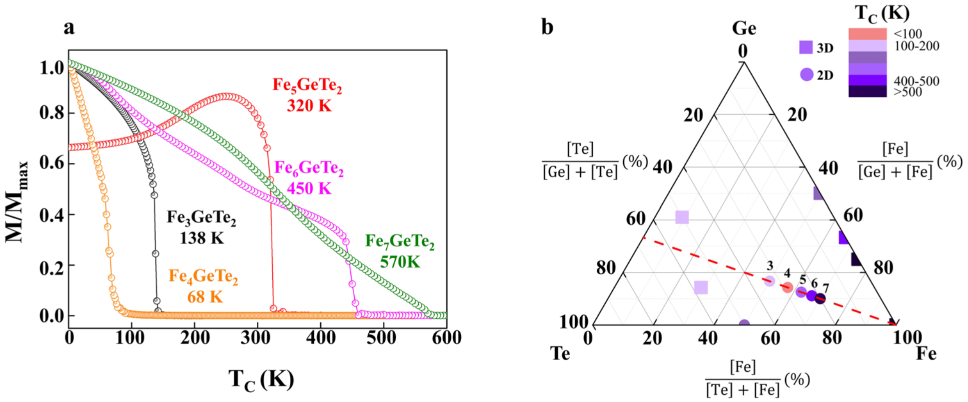

Fig. 4 Thickness-dependent magnetic properties of multilayer Fe_nGeTe_2 and comparison with other Fe-rich ferromagnets. a Calculated normalized magnetization of Fe atoms in Fe_nGeTe_2 as a function of temperature from Monte Carlo simulation. The M_{max} and T_C represent the maximum of magnetization and Curie temperature, respectively. **b** Ternary phase diagram of various Fe-rich compositions, together with the stoichiometric line of Fe:Ge:Te = n:1:2 ($3 \le n \le 7$). The color indicate the values of T_C. The squares and circles represent 3D and 2D structures, respectively.

(see Supplementary Note 5). For Fe^{2+}/Fe^{3+} ratios up to 0.5, the magnitude and sign of the coupling are insensitive to the distance between magnetic ion pairs, and there obviously exists competition between localized and itinerant magnetism. As the Fe^{2+}/Fe^{3+} ratio is increased further, localized magnetic exchange becomes dominant, and the magnitude decreases with the distance between Fe ions. Meanwhile, the variations in J_1, J_2, and J_3 can also be interpreted in terms of the magnetic interaction mechanism, as has earlier been established for 2D Fe_3GeTe_2.

To further clarify the magnetic ground states of 2D Fe_nGeTe_2 ultrathin films, the relationship between the exchange-path-dependent parameters J_1, J_2, and J_3 and the Fe^{2+}/Fe^{3+} ratio x is displayed in Fig. 3b, from which we can deduce several arguments. First, because the exchanges through d_{z^2} and d_{xz}/d_{yz} orbitals are dominant in multilayer structures, the interlayer localized d_{z^2} orbital interactions ($\boldsymbol{P_1}$, $\boldsymbol{P_2}$, and $\boldsymbol{P_3}$ paths) and the itinerant electron coupling of d_{xz}/d_{yz} orbitals ($\boldsymbol{I_2}$) are stronger than the intralayer interactions ($\boldsymbol{I_1}$ path) in Fe_nGeTe_2 systems. Second, for all the Fe_nGeTe_2 systems considered here, the dominant J parameter for FM coupling comes mainly from double exchange of localized d_{z^2} orbitals ($\boldsymbol{P_1}$ path) and coupling of itinerant electrons in d_{xz}/d_{yz} orbitals ($\boldsymbol{I_2}$). However, the major J parameter for AFM ordering comes mainly from coupling between localized d_{z^2} orbitals in Fe^{3+}–Fe^{3+} and Fe^{2+}–Fe^{2+} exchange ($\boldsymbol{P_2}$ and $\boldsymbol{P_3}$ paths). Therefore, the competition between interlayer AFM and FM coupling results from that between itinerant and localized magnetism in Fe^{2+}–Fe^{2+} or Fe^{3+}–Fe^{3+} coupling. In an Fe_5GeTe_2 ultrathin film, when the distance between interlayer Fe layers is shorter, the localized magnetic exchange through the $\boldsymbol{P_2}$ path can compete with itinerant e_2 electrons. However, the itinerant e_2 electrons become dominant as the Fe–Fe distance increases, such that the value of J_4 becomes 5.9 meV. Subsequently, the itinerant magnetism weakens as the Fe–Fe distance continues to increase, with the value of J_5 becoming 0.1 meV. Two competing ferromagnetisms of localized and itinerant are responsible for these complicated behaviors of the magnetic exchange parameters. As the Fe^{2+}/Fe^{3+} ratio increases, the itinerant behavior of d orbitals is weakened. That is to say, more localized $\boldsymbol{P_1}/\boldsymbol{P_3}$ paths (FM/AFM) and fewer $\boldsymbol{I_2}$ (FM) appear. Therefore, there is no simple trend of variation of the J parameters.

The MAE values for all the Fe_nGeTe_2 ultrathin films with different Fe^{2+}/Fe^{3+} ratios are also shown in Fig. 3a. One can see that MAE first increases from 0.91 meV/Fe atom for $x = 0$ (Fe_5GeTe_2) to 1.05 meV/Fe atom for $x = 0.2$ (Fe_6GeTe_2). Then, it decreases almost monotonically with increasing Fe^{2+}/Fe^{3+} ratio in the mixed-valence Fe_nGeTe_2 compounds. As x further increases to 1, the easy axis flips from a perpendicular into an in-plane orientation. The amplitude and direction of magnetic anisotropy are affected by two competing factors simultaneously. One is the Fe^{2+}/Fe^{3+} ratio. As we have discussed with regard to 2D Fe_3GeTe_2, the Fe^{3+} and Fe^{2+} ions contribute to positive and negative MAE, respectively. Another important factor is the interaction between d_{z^2} and d_{xz}/d_{yz} orbitals, since the electronic band structures reveal that the spin-minority components of these orbitals are affected by SOC associated with the inserted Fe layers. To further unveil the origin of MAE enhancement from Fe_5GeTe_2 to Fe_6GeTe_2, we decompose the MAE into the coupling of d_{z^2} and d_{xz}/d_{yz} pairs by Eq. (4) (see Supplementary Fig. 10). When the Fe^{2+}/Fe^{3+} ratio is 0 (Fe_5GeTe_2), there exist only positive contributions of occupied d_{xz}/d_{yz} and unoccupied d_{z^2} pairs, with a difference in orbital energy levels of about 4.08 eV, leading to an out-of-plane MAE of 0.91 meV/Fe atom. When the Fe^{2+}/Fe^{3+} ratio is increased from 0 (Fe_5GeTe_2) to 0.2 (Fe_6GeTe_2), the energy level differences between occupied d_{xz}/d_{yz} and unoccupied d_{z^2} pairs and unoccupied d_{xz}/d_{yz} and occupied d_{z^2} pairs become 3.79 and 4.65 eV, respectively. Therefore, for the occupied d_{xz}/d_{yz} and unoccupied d_{z^2} pairs, the positive contributions to MAE prevail over the negative contributions.

Based on the obtained magnetic exchange constants and MAE, the Curie temperature of Fe_nGeTe_2 is estimated using the 2D Heisenberg model, as shown in Fig. 4a. We have also simulated the M–T curves for every Fe sublattice (see Supplementary Fig. 11). The obtained T_C value of 138 K for 2D Fe_3GeTe_2 coincides well with previous experimental values of about 68–130 K[13,14]. The temperature-dependent magnetic moments (i.e., M–T curves) for each type of Fe ion (Fe^{3+} and Fe^{2+}) in Fe_3GeTe_2 compounds are also presented in Supplementary Fig. 11a. One can see that the magnetizations of both Fe^{3+} and Fe^{2+} sublattices indeed behave like ferromagnets. Additionally, the estimated T_C for bulk Fe_3GeTe_2 crystal is 280 K (see Supplementary Note 5), which is also comparable to the experimental value of 230 K[27].

For various stoichiometries, three kinds of M–T curves are observed. Similar to Fe_3GeTe_2, Fe_4GeTe_2 is also a true ferromagnet. The magnetic spin moments of all Fe atoms align in the same direction, and they decrease with increasing temperature, yielding a T_C value of 68 K. One should note that this T_C is significantly lower than the experimentally reported one (270 K), owing to differences in thickness and symmetry[15]. For Fe_5GeTe_2, the magnetic moment continues to increase with temperature, and full compensation is not observed anywhere in the entire temperature range. The maximum in spontaneous magnetization appears between 0 K and T_C (320 K). For each Fe sublattice, the Fe_1 and Fe_5 layers are thermally disturbed more easily, and their magnetic moments decrease almost linearly with increasing temperature, while the other three layers (Fe_2, Fe_3, and Fe_4) drastically decrease around 320 K. The correlation here between magnetization and temperature is characteristic of a Néel's P-type ferrimagnet[50]. The ferrimagnetic (FiM)-to-paramagnetic transition occurs at a critical temperature $T_C = 320$ K. Such complicated magnetic behavior of Fe_5GeTe_2 has also been discussed in previous papers. For example, Ramesh et al.[51] found that the $Fe_{5-x}GeTe_2$ system exhibited a temperature-dependent FM-to-FiM phase transition, and existed glassy cluster behavior at low temperature. Li et al.[22] performed spin dynamics simulations of Fe_5GeTe_2, the results of which support the existence of the magnetic transition but not that of a spin glass state. Compared with 2D $Fe_{5-x}GeTe_2$, Fe_6GeTe_2 and Fe_7GeTe_2 sheets exhibit a relatively rapid decline in magnetization within an intermediate range of temperatures, showing the characteristics of a Néel's R-type ferrimagnet. From a careful analysis of the spin coupling strength, we speculate that the main feature distinguishing FiM Fe_5GeTe_2 from Fe_6GeTe_2 and Fe_7GeTe_2 is the existence of a frustration effect. In this situation, the magnetic moments of Fe_5GeTe_2 will be more sensitive to the thermal fluctuations induced by temperature.

The M–T curves exhibit monotonic decreases with increasing temperature. For the Fe sublattices of Fe_6GeTe_2, the spin moments of the Fe_1, Fe_3, Fe_4, Fe_5, and Fe_6 layers and those of the Fe_2 layers show opposite directions, although all the moments decrease with temperature. For the M–T curves of 2D Fe_7GeTe_2, the spin directions of the Fe_2, Fe_4, and Fe_5 layers and those of the Fe_1, Fe_3, Fe_6, and Fe_7 layers are opposite. The FiM-to-paramagnetic transition occurs at a T_C of 570 K. The Néel's R- and P-type magnetization profiles seen here have also been reported in mixed-valence complex alloys ($Mn_{1.5}FeV_{0.5}Al$[52] and $Mn_2V_{0.5}C_{0.5}Z$[53]), complex oxides ($NiCo_2O_4$[54]), layered materials ($AFe^{II}Fe^{III}(C_2O_4)_3$[55]) and core–shell nanoparticles[56]. The competition between interlayer AFM and FM coupling resulting in the transition from FM to FiM states in Fe_nGeTe_2 is derived from the coexistence of different electronic states.

The simulated values of T_C are 138 K for Fe_3GeTe_2, 68 K for Fe_4GeTe_2, 320 K for Fe_5GeTe_2, 450 K for Fe_6GeTe_2, and 570 K for Fe_7GeTe_2. For truly FM systems, T_C drops from 138 K for Fe_3GeTe_2 to 68 K for Fe_4GeTe_2 because of the flipping of out-of-plane MAE brought about by the increased ratio of Fe^{2+} ions. Further increases in Fe content lead to a transition of magnetic ordering from FM to FiM at Fe_5GeTe_2. For $n \geq 5$, the T_C of the FiM Fe_nGeTe_2 film increases with n, mainly owing to the higher MAE and stronger double exchange. A similar trend has also been observed in FM $Fe_{3-x}Cr_xGe$ and $Fe_{3-x}V_xGe$ alloys[57,58]. Extrapolating to even thicker films, Fe_nGeTe_2 with $n = 9$ and an effective thickness of 14 Å yields a $T_C = 1006$ K, which is comparable to the $T_C = 1043$ K for pure Fe solid of bcc phase[15] (see Supplementary Fig. 13).

To provide a more general view of the composition and dimensional effects on the magnetic behavior of Fe–Ge–Te systems, we plot a ternary phase diagram of T_C for various reported Fe-based compounds (Fig. 4b). In the three-dimensional (3D) compounds, the T_C of Fe-rich compositions increases monotonically from 279 K for FeGe[59] to 485 K for Fe_2Ge[60], and then to 1043 K for pure Fe[15], revealing a prominent composition effect. In the 2D Fe–Ge–Te films, T_C is determined by a combination of composition and dimensional effects. Generally speaking, incorporation of Fe atoms into the system will increase T_C. For example, Fe doping generates long-range spin ordering in GeTe films, and the T_C of $Fe_{0.18}Ge_{0.82}Te$ films is 100 K[61]. The T_C of our Fe_3GeTe_2 with an effective thickness of 0.86 nm (138 K) is lower than that of an FeTe ultrathin film with thickness 2.80 nm ($T_C = 220$ K)[12], even with the same Fe content. Moreover, the T_C of Fe_6GeTe_2 (450 K) is slightly lower than that of the bulk Fe_2Ge phase ($T_C = 485$ K). Both of them have an Fe content of 0.67. However, the role of nonmetal element (Ge and Te) inclusions in ultrathin Fe–Ge–Te films is very complicated. These inclusions can not only tune the chemical valence state and the electronic behavior of the variable element Fe, but also provide a crystal field to control the MAE, which will change the magnetic behavior and T_C.

Conclusion

We have designed a family of 2D Fe_nGeTe_2 ultrathin films with different Fe contents and thicknesses, which are experimentally more feasible than the reported 2D layered phase. By first-principles calculations, we have systemically studied their electronic and magnetic properties and have some important findings to obtain low-dimensional magnetic materials with high working temperature. All the 2D Fe_nGeTe_2 ultrathin films considered here are robust ferromagnetic/ferrimagnetic materials with magnetic transition temperatures of 68–570 K, which can be ascribed to the coexistence of itinerant and localized electronic states. The localized magnetism comes from the electrons in d_{z^2} orbital, while the itinerant magnetism derives from electrons in $d_{xz}/d_{yz}/d_{xy}/d_{x^2-y^2}$ orbitals. The coexistence of itinerant and localized electronic states is also correlated well with the values of many critical magnetic parameters, such as magnetic moment, exchange parameters, MAE, and T_C, all of which have been discussed in detail in this paper. Based on these results, we have proposed a localized Fe–Fe exchange Heisenberg model that provides a good description of the exchange between d_{z^2} orbitals in Fe–Ge–Te systems. It may also be appropriate for application to variable-valence element-based magnetic compounds. Meanwhile, the itinerant magnetism introduced to our mechanism to explain the competitive intra- and interlayer ferromagnetism. Moreover, the established thickness-dependent magnetic order suggests the possibility of tuning the interlayer exchange energy of Fe–Ge–Te systems by changing the composition. The results of this study should prove very helpful in further understanding the modulating effect of thickness on 2D Fe_nGeTe_2 ultrathin films with variable-valence elements. They also indicate that 2D magnetic Fe_nGeTe_2 ultrathin films are promising candidates for future room-temperature spintronic applications.

Methods

Electronic band structure calculation. Our first-principles calculations were based on density functional theory (DFT) within the generalized gradient approximation (GGA)[62], as implemented in the VASP code[63]. The projected augmented wave (PAW) potential was used to describe ion–electron interaction[64]. The energy cutoff of the plane-wave basis was set as 500 eV. A vacuum space of 20 Å thickness was added to avoid interaction between adjacent layers. During geometry optimization, a Monkhorst–Pack **k**-point mesh of 0.02 $Å^{-1}$ was chosen for sampling the 2D Brillouin zones. To remove self-interaction errors, the effective Hubbard U parameter ($U = 4.3$ eV) was included within the PBE+U framework, which is consistent with previous studies[65,66]. Different U values at various Fe^{2+}/Fe^{3+} ratios x were also tested, as shown in Supplementary Note 5. Our results shown that the best choice for all Fe_nGeTe_2 compounds is $U = 4.3$, although a different value would not affect our conclusions. Correction of van der Waals interactions using the DFT-D3 scheme[67] was included in the bulk Fe_3GeTe_2 calculations.

Magnetic parameters. To describe the magnetic properties of Fe_nGeTe_2 crystals, the magnetic anisotropy energy (MAE) is defined as

$$\mathrm{MAE} = E_{\mathrm{tot}}[100] - E_{\mathrm{tot}}[001], \quad (2)$$

where $E_{\mathrm{tot}}[100]$ and $E_{\mathrm{tot}}[001]$ are to the total energies of states whose magnetization direction is parallel and perpendicular to the basal plane, respectively[68]. The MAE is determined by considering the SOC effect through noncollinear calculations.

In the present system, the minority spin states dominate the magnetic anisotropy, and so the MAE can be expressed as[69]

$$\mathrm{MAE} \approx \triangle E^{\mathrm{dd}} = \xi^2 \sum_{o^- u^-} \frac{\left|\left\langle o^-, |, L_z, |, u^- \right\rangle\right|^2 - \left|\left\langle o^-, |, L_x, |, u^- \right\rangle\right|^2}{\varepsilon_{u^-} - \varepsilon_{o^-}}. \quad (3)$$

Here, L_x and L_z are the x and z components of the angular momentum operator, and o and u denote the spin-down orbitals in the occupied and unoccupied states, respectively. From Eq. (3), we can see that $\triangle E^{\mathrm{dd}}$ is not only determined by the orbital character of the occupied states, but also depends on the coupling with the empty states and the splitting between them through the energy denominator. For a simple analysis, we decompose Eq. (3) into matrix elements with the Fe-d orbitals that predominant near the Fermi level in spin-down states, omitting the SOC constant[70]. The MAE can then be expressed approximately as

$$\mathrm{MAE}^{\mathrm{dd}} \approx \frac{\left|\left\langle xz, |, L_z, |, yz \right\rangle\right|^2}{\varepsilon_{xz} - \varepsilon_{yz}} - \frac{\left|\left\langle xz, yz, |, L_x, |, z^2 \right\rangle\right|^2}{\varepsilon_{xz,yz} - \varepsilon_{z^2}}. \quad (4)$$

Monte Carlo simulations. Monte Carlo simulations were carried out to determine the magnetic transition temperatures. The Hamiltonian of the system was expressed as follows:

$$\mathcal{H} = -\sum_{\langle ij \rangle} J_{ij} \mathbf{S}_i \cdot \mathbf{S}_j - K \sum_i (\mathbf{S}_i \cdot \mathbf{e}_i)^2, \quad (5)$$

where $\mathbf{S}_i$ is the unit vector of the magnetic moment at site i, J_{ij} is the exchange-coupling constant between magnetic Fe atoms, K is the anisotropy constant, and $\mathbf{e}_i$ is the unit vector along the easy direction of the magnetic anisotropy. The parameters used in the MC simulations were obtained from first-principles calculations. To determine the Curie temperature, the magnetization M per atom and the specific heat C_{m} were calculated by

$$M = \frac{1}{N} \langle [(\sum_i S_i^x)^2 + (\sum_i S_i^y)^2 + (\sum_i S_i^z)^2]^{1/2} \rangle \quad (6)$$

and

$$C_{\mathrm{m}} = \frac{\langle E^2 \rangle - \langle E \rangle^2}{N k_{\mathrm{B}} T^2}, \quad (7)$$

respectively. Here, N is the total number of magnetic Fe atoms, and k_{B} is the Boltzmann constant. The simulation supercells were constructed by 50×50 expansion of the unit cell. For each temperature, the first 10^5 MC steps were discarded for thermal equilibration, and the successive 10^5 MC steps were then used to collect data and determine the thermodynamic averages of given physical quantities. All thermodynamic properties were averaged over five different seed numbers.

Data availability

The data that support the findings of this study are available from the corresponding author on reasonable request.

Code availability

The electronic structure and magnetic properties calculations were performed using the proprietary code VASP[63]. The codes of Monte Carlo simulations in this paper are available from the authors upon request.

Received: 9 October 2021; Accepted: 19 May 2022;
Published online: 03 June 2022

References

1. Huang, B. et al. Layer-dependent ferromagnetism in a van der Waals crystal down to the monolayer limit. *Nature* **546**, 270–273 (2017).
2. McGuire, M. Crystal and magnetic structures in layered, transition metal dihalides and trihalides. *Crystals* **7**, 121 (2017).
3. Li, Z., Zhou, B. & Luan, C. Strain-tunable magnetic anisotropy in two-dimensional Dirac half-metals: nickel trihalides. *RSC Adv.* **9**, 35614–35623 (2019).
4. Gong, C. et al. Discovery of intrinsic ferromagnetism in two-dimensional van der Waals crystals. *Nature* **546**, 265–269 (2017).
5. Vatansever, E. et al. Strain effects on electronic and magnetic properties of the monolayer α-$RuCl_3$: A first-principles and Monte Carlo study. *J. Appl. Phys.* **125**, 083903 (2019).
6. Ersan, F. et al. Exploring the electronic and magnetic properties of new metal halides from bulk to two-dimensional monolayer: RuX_3 (X = Br, I). *J. Magn. Magn. Mater.* **476**, 111–119 (2019).
7. Goodenough, J. B. Theory of the role of covalence in the perovskite-type manganites [La, *M*(II)]MnO_3. *Phys. Rev.* **100**, 564–573 (1955).
8. Kanamori, J. Crystal distortion in magnetic compounds. *J. Appl. Phys.* **31**, S14–S23 (1960).
9. Anderson, P. W. New approach to the theory of superexchange interactions. *Phys. Rev.* **115**, 2–13 (1959).
10. Bhatti, S. et al. Spintronics based random access memory: a review. *Mater. Today* **20**, 530–548 (2017).
11. Zhang, Y. et al. Ultrathin magnetic 2D single-crystal CrSe. *Adv. Mater.* **31**, 1900056 (2019).
12. Kang, L. et al. Phase-controllable growth of ultrathin 2D magnetic FeTe crystals. *Nat. Commun.* **11**, 3729 (2020).
13. Fei, Z. et al. Two-dimensional itinerant ferromagnetism in atomically thin Fe_3GeTe_2. *Nat. Mater.* **17**, 778–782 (2018).
14. Deng, Y. et al. Gate-tunable room-temperature ferromagnetism in two-dimensional Fe_3GeTe_2. *Nature* **563**, 94–99 (2018).
15. Seo, J. et al. Nearly room temperature ferromagnetism in a magnetic metal-rich van der Waals metal. *Sci. Adv.* **6**, eaay8912 (2020).
16. May, A. F. et al. Ferromagnetism near room temperature in the cleavable van der waals crystal Fe_5GeTe_2. *ACS Nano* **13**, 4436–4442 (2019).
17. Yuan, Q.-Q. et al. Ferromagnetic MnSn monolayer epitaxially grown on silicon substrate. *Chin. Phys. Lett.* **37**, 077502 (2020).
18. Abdullahi, Y. Z. et al. Ferromagnetic TM_2BC (TM = Cr, Mn) monolayers for spintronic devices with high Curie temperature. *Phys. Chem. Chem. Phys.* **23**, 6107–6115 (2021).
19. Gökoğlu, G. & Aktürk, E. Half metallicity and pressure-induced electronic structure of monolayer FeX_2 (X = S, Se). *Mater. Res. Express* **4**, 116305 (2017).
20. Wu, H. et al. Strong intrinsic room-temperature ferromagnetism in freestanding non-van der Waals ultrathin 2D crystals. *Nat. Commun.* **12**, 5688 (2021).
21. Meng, L. et al. Anomalous thickness dependence of Curie temperature in air-stable two-dimensional ferromagnetic 1*T*-$CrTe_2$ grown by chemical vapor deposition. *Nat. Commun.* **12**, 809 (2021).
22. Alahmed, L. et al. Magnetism and spin dynamics in room-temperature van der Waals magnet Fe_5GeTe_2. *2D Mater.* **8**, 045030 (2021).
23. Stoner, E. C. Collective electron ferronmagnetism. *Proc. R. Soc. Lond. Ser. A. Math. Phys. Sci.* **165**, 372–414 (1938).
24. Wang, H. et al. Pressure-dependent intermediate magnetic phase in thin Fe_3GeTe_2 flakes. *J. Phys. Chem. Lett.* **11**, 7313–7319 (2020).
25. Xu, X. et al. Signature for non-Stoner ferromagnetism in the van der Waals ferromagnet Fe_3GeTe_2. *Phys. Rev. B* **101**, 201104 (2020).
26. Henkelman, G., Arnaldsson, A. & Jónsson, H. A fast and robust algorithm for Bader decomposition of charge density. *Comp. Mater. Sci.* **36**, 354–360 (2006).
27. Deiseroth, H.-J., Aleksandrov, K., Reiner, C., Kienle, L. & Kremer, R. K. Fe_3GeTe_2 and Ni_3GeTe_2 – two new layered transition-metal compounds: crystal structures, HRTEM investigations, and magnetic and electrical properties. *Eur. J. Inorg. Chem.* **2006**, 1561–1567 (2006).
28. Kou, S.-P., Li, T. & Weng, Z.-Y. Coexistence of itinerant electrons and local moments in iron-based superconductors. *Europhys. Lett.* **88**, 17010 (2009).
29. Tovar, M. et al. Evidence of strong antiferromagnetic coupling between localized and itinerant electrons in ferromagnetic Sr_2FeMoO_6. *Phys. Rev. B* **66**, 024409 (2002).
30. Edwards, D. M. Ferromagnetism and electron-phonon coupling in the manganites. *Adv. Phys.* **51**, 1259–1318 (2002).
31. Bhide, V. G., Rajoria, D. S., Rao, C. N. R., Rao, G. R. & Jadhao, V. G. Itinerant-electron ferromagnetism in $La_{1-x}Sr_xCoO_3$: A Mössbauer study. *Phys. Rev. B* **12**, 2832–2843 (1975).
32. Ming, X. et al. Unusual intermediate spin Fe^{3+} ion in antiferromagnetic Li_3FeN_2. *J. Appl. Phys.* **111**, 063704 (2012).
33. Feng, X. et al. Slow magnetic relaxation in intermediate Spin $S = 3/2$ mononuclear Fe(III) complexes. *J. Am. Chem. Soc.* **139**, 16474–16477 (2017).
34. Li, Z. et al. The marriage of the FeN_4 moiety and MXene boosts oxygen reduction catalysis: Fe 3d electron delocalization matters. *Adv. Mater.* **30**, 1803220 (2018).
35. Potze, R. H., Sawatzky, G. A. & Abbate, M. Possibility for an intermediate-spin ground state in the charge-transfer material $SrCoO_3$. *Phys. Rev. B* **51**, 11501–11506 (1995).
36. Zhu, J.-X. et al. Electronic correlation and magnetism in the ferromagnetic metal Fe_3GeTe_2. *Phys. Rev. B* **93**, 144404 (2016).
37. Stöhr, J. & Siegmann, H. C. *Magnetism* (Springer-Verlag, Berlin, Germany, 2006).
38. Moritomo, Y., Asamitsu, A. & Tokura, Y. Pressure effect on the double-exchange ferromagnet $La_{1-x}Sr_xMnO_3$ (0.15< = x< = 0.5). *Phys. Rev. B* **51**, 16491–16494 (1995).

39. Yi, J. et al. Competing antiferromagnetism in a quasi-2D itinerant ferromagnet: Fe_3GeTe_2. *2D Mater.* **4**, 011005 (2016).
40. Fu, Z., Chen, H., Liu, Y., Liu, M. & Liu, W.-M. Interface-induced ferroelectric domains and charged domain walls in $BiFeO_3/SrTiO_3$ superlattices. *Phys. Rev. B* **103**, 195301 (2021).
41. Hu, X. et al. Enhanced ferromagnetism and tunable magnetism in Fe_3GeTe_2 monolayer by strain engineering. *ACS Appl. Mater. Inter.* **12**, 26367–26373 (2020).
42. Shabbir, B. et al. Long range intrinsic ferromagnetism in two dimensional materials and dissipationless future technologies. *Appl. Phys. Rev.* **5**, 041105 (2018).
43. Wang, P., Jiang, X., Hu, J. & Zhao, J. Chemically engineering magnetic anisotropy of 2D metalloporphyrin. *Adv. Sci.* **4**, 1700019 (2017).
44. Park, S. Y. et al. Controlling the magnetic anisotropy of the van der waals ferromagnet Fe_3GeTe_2 through hole doping. *Nano Lett.* **20**, 95–100 (2020).
45. Kim, D. et al. Antiferromagnetic coupling of van der Waals ferromagnetic Fe_3GeTe_2. *Nanotechnology* **30**, 245701 (2019).
46. May, A. F., Calder, S., Cantoni, C., Cao, H. & McGuire, M. A. Magnetic structure and phase stability of the van der Waals bonded ferromagnet $Fe_{3-x}GeTe_2$. *Phys. Rev. B* **93**, 014411 (2016).
47. Villars, P., Calvert, L. D. & Pearson, W. B. Handbook of crystallographic data for intermetallic phases. *Acta Crystallogr. A* **40**, C444 (1984).
48. Jain, A. et al. Commentary: the materials project: A materials genome approach to accelerating materials innovation. *APL Mater.* **1**, 011002 (2013).
49. Chu, J. et al. Sub-millimeter-scale growth of one-unit-cell-thick ferrimagnetic Cr_2S_3 nanosheets. *Nano Lett.* **19**, 2154–2161 (2019).
50. Néel, M. L. Propriétés magnétiques des ferrites ; ferrimagnétisme et antiferromagnétisme. *Ann. Phys.* **12**, 137–198 (1948).
51. Zhang, H. et al. Itinerant ferromagnetism in van der Waals $Fe_{5-x}GeTe_2$ crystals above room temperature. *Phys. Rev. B* **102**, 064417 (2020).
52. Stinshoff, R. et al. Completely compensated ferrimagnetism and sublattice spin crossing in the half-metallic Heusler compound $Mn_{1.5}FeV_{0.5}Al$. *Phys. Rev. B* **95**, 060410 (2017).
53. Midhunlal, P. V., Arout Chelvane, J., Prabhu, D., Gopalan, R. & Harish Kumar, N. $Mn_2V_{0.5}Co_{0.5}Z$ (Z = Ga, Al) Heusler alloys: High T_C compensated P-type ferrimagnetism in arc melted bulk and N-type ferrimagnetism in melt-spun ribbons. *J. Magn. Magn. Mater.* **489**, 165298 (2019).
54. Bitla, Y. et al. Origin of metallic behavior in $NiCo_2O_4$ ferrimagnet. *Sci. Rep.-UK* **5**, 15201 (2015).
55. Nuttall, C. J. & Day, P. Magnetization of the layer compounds $AFe^{II}Fe^{III}(C_2O_4)_3$ (A = Organic Cation), in low and high magnetic fields: Manifestation of Néel N and Q type ferrimagnetism in a molecular lattice. *Chem. Mater.* **10**, 3050–3057 (1998).
56. Vatansever, E. & Polat, H. Monte Carlo investigation of a spherical ferrimagnetic core–shell nanoparticle under a time dependent magnetic field. *J. Magn. Magn. Mater.* **343**, 221–227 (2013).
57. Mahat, R. et al. Tuneable structure and magnetic properties in $Fe_{3-x}V_x$ Ge alloys. *J. Alloy. Compd.* **830**, 154403 (2020).
58. Mahat, R. et al. Influence of Cr-substitution on the structural, magnetic, electron transport, and mechanical properties of $Fe_{3-x}Cr_xGe$ Heusler alloys. *J. Magn. Magn. Mater.* **521**, 167398 (2021).
59. Xu, L. et al. Magnetic entropy change and accurate determination of Curie temperature in single-crystalline helimagnet FeGe. *Europhys. Lett.* **117**, 47004 (2017).
60. Yasukōchi, K., Kanematsu, K. & Ohoyama, T. Magnetic properties of intermetallic compounds in iron-germanium system : $Fe_{1.67}Ge$ and $FeGe_2$. *J. Phys. Soc. Jpn.* **16**, 429–433 (1961).
61. Fukuma, Y., Asada, H., Miyashita, J., Nishimura, N. & Koyanagi, T. Magnetic properties of IV–VI compound GeTe based diluted magnetic semiconductors. *J. Appl. Phys.* **93**, 7667–7669 (2003).
62. Perdew, J. P., Burke, K. & Ernzerhof, M. Generalized gradient approximation made simple. *Phys. Rev. Lett.* **77**, 3865–3868 (1996).
63. Hafner, J. Ab-initio simulations of materials using VASP: Density-functional theory and beyond. *J. Comput. Chem.* **29**, 2044–2078 (2008).
64. Blochl, P. E. Projector augmented-wave method. *Phys. Rev. B* **50**, 17953–17979 (1994).
65. Mosey, N. J., Liao, P. & Carter, E. A. Rotationally invariant ab initio evaluation of Coulomb and exchange parameters for DFT+U calculations. *J. Chem. Phys.* **129**, 014103 (2008).
66. Zhuang, H. L., Kent, P. R. C. & Hennig, R. G. Strong anisotropy and magnetostriction in the two-dimensional Stoner ferromagnet Fe_3GeTe_2. *Phys. Rev. B* **93**, 134407 (2016).
67. Grimme, S., Antony, J., Ehrlich, S. & Krieg, H. A consistent and accurate ab initio parametrization of density functional dispersion correction (DFT-D) for the 94 elements H-Pu. *J. Chem. Phys.* **132**, 154104 (2010).
68. Abdullahi, Y. Z., Ersan, F., Vatansever, Z. D., Aktürk, E. & Aktürk, O. Ü. Exploring the potential of MnX (S, Sb) monolayers for antiferromagnetic spintronics: A theoretical investigation. *J. Appl. Phys.* **128**, 113903 (2020).
69. Xing, J. et al. Rational design of 2D organic magnets with giant magnetic anisotropy based on two-coordinate 5d transition metals. *APL Mater.* **8**, 071105 (2020).
70. Odkhuu, D. Magnetization reversal of giant perpendicular magnetic anisotropy at the magnetic-phase transition in FeRh films on MgO. *Phys. Rev. B* **93**, 064412 (2016).

Acknowledgements

This work was supported by the National Natural Science Foundation of China (11874097, 91961204, 11804044, and 12004065) and the Genetic Engineering of Precious Metal Materials in Yunnan Province (I)-Construction and Application of Precious Metal Materials Professional Database (I) (202002AB080001-1). The authors also acknowledge the Supercomputing Center of Dalian University of Technology for providing the computing resources.

Author contributions

X.J. supervised this study. X.J., Y.Q., and J.J.Z. conceived the idea. Q.X.L. and Y.Q. performed the theoretical simulations. J.P.X., Z.J., and Y.G. participated in the discussion of results. X.J. and Q.X.L. drafted the manuscript. J.J.Z. edited the manuscript. All the authors contributed to the overall scientific interpretation.

Competing interests

The authors declare no competing interests.

Additional information

Supplementary information The online version contains supplementary material available at https://doi.org/10.1038/s42005-022-00921-3.

Correspondence and requests for materials should be addressed to Xue Jiang or Yan Qi.

Peer review information *Communications Physics* thanks the anonymous reviewers for their contribution to the peer review of this work. Peer reviewer reports are available.

Reprints and permission information is available at http://www.nature.com/reprints

Publisher's note Springer Nature remains neutral with regard to jurisdictional claims in published maps and institutional affiliations.